IPEM Institute of Physics and Engineering in Medicine

Quantification of myocardial uptake rate constants in dynamic small-animal SPECT using a cardiac phantom

Quantification of Myocardial Uptake Rate Constants in Dynamic Small-Animal SPECT using a Cardiac Phantom

Lindsay C. Johnson[1], Marie A. Guerraty[2], Stephen C. Moore[1], Scott D. Metzler[1]

[1] University of Pennsylvania Perelman School of Medicine, Department of Radiology
[2] University of Pennsylvania Perelman School of Medicine, Division of Cardiovascular Medicine

Abstract

Myocardial blood flow and myocardial blood flow reserve (MBFR) measurements are often used clinically to quantify coronary microvascular function. Developing imaging-based methods to measure MBFR for research in mice would be advantageous for evaluating new treatment methods for coronary microvascular disease, yet this is more challenging in mice than in humans. This work investigates microSPECT's quantitative capabilities of cardiac imaging by utilizing a multi-part cardiac phantom and applying a known kinetic model to synthesize kinetic data from static data, allowing for assessment of kinetic modeling accuracy. The phantom was designed with four main components: two left-ventricular (LV) myocardial sections and two LV blood-pool sections, sized for end-systole and end-diastole. Each section of the phantom was imaged separately while acquiring list-mode data. These static, separate-compartment data were manipulated into synthetic dynamic data using a kinetic model representing the myocardium and blood-pool activity concentrations over time and then combined into a set of dynamic image frames and reconstructed. Regions of interest were drawn on the resulting images, and kinetic parameters were estimated. This process was performed for three tracer uptake values (K_1), three myocardial wall thicknesses, 10 filter parameters, and 20 iterations for 25 noise ensembles. The degree of filtering and iteration number were optimized to minimize the root mean-squared error (RMSE) of K_1 values, with the largest number of iterations and minimal filtering yielding the lowest error. Using the optimized parameters, K_1 was determined with reasonable error ($\sim$3% RMSE) over all wall thicknesses and K_1 input values. This work demonstrates that accurate and precise measurements of K_1 are possible for the U-SPECT+ system used in this study, for several different uptake rates and LV dimensions. Additionally, it allows for future investigation utilizing other imaging systems, including PET studies with any radiotracer, as well as with additional phantom parts containing lesions.

1. Introduction

Coronary microvascular disease (CMVD), or disease of the coronary pre-arterioles and arterioles, has become an increasingly well-recognized cardiac pathology (Camici and Crea 2007) which contributes significantly to cardiac morbidity and mortality (Bairey Merz *et al.*, 2017; Gibson *et al.*, 2000). The coronary microvasculature regulates myocardial blood flow (MBF) in response to metabolic demand and is critical in maintaining proper myocardial perfusion. MBF increases in response to cardiac stressors, such as exercise or pharmacologic vasodilators. In the absence of flow-limiting epicardial coronary artery lesions, the ability to increase MBF is a direct measure of coronary microvascular function (Ahmed, 2014). This is typically quantified using the metric of myocardial blood flow reserve (MBFR), which is defined as the ratio of MBF at stress to MBF at rest. Studies have shown that diminished MBFR is correlated with poor cardiovascular outcomes in various populations (Majmudar *et al.*, 2015; Murthy *et*

2

al., 2014), and that determining MBF and MBFR improve the diagnostic and prognostic value over myocardial perfusion imaging alone (Farhad *et al.*, 2013; Herzog *et al.*, 2009).

Developing methods based on imaging to measure MBF and MBFR for research in small animals such as mice would be advantageous for evaluating new treatment methods for CMVD. However, such measurements are currently challenging using mice due to their small size, even when utilizing dedicated small-animal systems. Currently, mouse studies of CMVD have been limited to structural studies or ex-vivo studies (Duncker and Bache, 2008; Moslehi *et al.*, 2010; Chintalgattu *et al.*, 2013). Although PET is more commonly used clinically, in small animal imaging microSPECT typically has superior spatial resolution to microPET due to the use of pinholes (Beekman and van der Have, 2007) and has less expensive tracers, making it better suited than PET for this particular application.

We are working to develop a non-invasive imaging technique to allow *in-vivo* and longitudinal evaluation of MBFR in mouse models of CMVD (Guerraty *et al.*, 2017). We have previously developed a protocol to image mice dynamically under rest and stress conditions on a microSPECT system in order to measure MBFR changes in wild type mice using customized kinetic modeling software (Johnson *et al.*, 2016); however, we currently lack a method to evaluate the quantitative accuracy of these studies, with regard to imaging and modeling errors. An example of this work is shown in Fig. 1, which shows slices of reconstructed images and a corresponding time activity curve of both the myocardium and the blood pool. The tracer uptake rate constant, K_1, which is necessary but not sufficient for determining MBF, should ideally be compared to some other "gold-standard" technique for evaluating quantitative accuracy. Although it is possible to estimate MBF in mice via invasive methods, such as using fluorescent microspheres, (Gervais *et al.*, 1999), additional factors are required to determine K_1 from MBF. Also, these MBF determination methods are terminal methods do not allow for longitudinal studies and are challenging to perform on the small scale of mice.
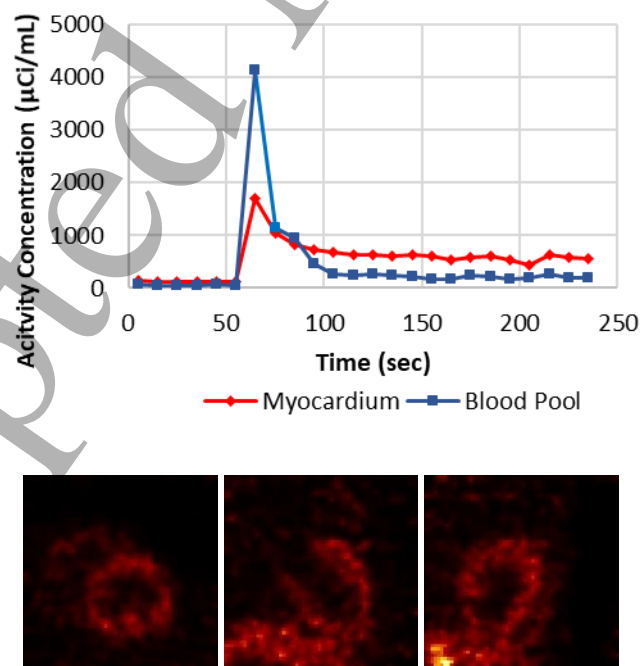

Fig. 1: An example of a previously acquired dynamic mouse acquisition. Top: the resulting time activity curve when data were reconstructed in 10-second frames. Bottom: image slices from a 60-second

acquisition starting at 320 seconds into the scan. These results show the approximate shape and distribution of activity concentration in the myocardium and blood pool over time, and is highly dependent on the amount of activity injected and the unknown K_1 of the subject.

In this work, we focus on evaluating the accuracy of rate constants determined from dynamic cardiac microSPECT by acquiring image data from a multi-compartment cardiac phantom to compute synthetic dynamic cardiac SPECT image frames, as well as corrections for resolution blurring and spillover (crosstalk) between the phantom's "myocardium" and its left ventricular "blood pool". This phantom study allows for a known K_1 to be compared to imaging results that include effects attributable to system noise, resolution, and kinetic modeling. Note that the determination of absolute MBF will ultimately also require correction for the tracer-specific extraction fraction (EXF) from arterial blood to myocardial tissue which, itself, varies nonlinearly with blood flow for all but freely diffusible tracers (e.g., $H_2^{15}O$). While the EXF and its flow dependence have been evaluated for several tracers in humans, they have not yet been well characterized for SPECT tracers in mice; this will be the subject of future research.

2. Methods

2.1. Phantom Description

We have designed and printed a three-dimensional (3D) multi-compartment cardiac phantom (printed by Solid Technologies, Inc. on an MJP ProJet 2500 system using VisiJet M2R-CL Rigid Clear material). The phantom has two sections each of left-ventricular myocardium and left-ventricular blood pool, with one section of each sized appropriately to represent end-diastole (ED), and the other for end-systole (ES), where myocardial volume is preserved between the two states. This configuration can be seen in Fig. 2. The ED blood pool was modeled as frustoconical with a cap that was a portion of an ellipsoid. The frustocone had length 5.8 mm and diameters of 2.5 mm and 2.3 mm at the basal and apical ends, respectively. The ellipsoidal cap replacing the tip of the truncated cone had diameters of 2.3 mm perpendicular to the cone's axis and 1.0 mm diameter along the cone's axis, giving a total length of 6.3 mm; the frustocone and ellipsoid had matching diameters and slopes at their intersection. Similarly, the ES blood pool was modeled as the same basic shape, but the frustocone had length 5.0 mm and diameters of 2.0 mm and 1.8 mm at the basal and apical ends, respectively. The ellipsoidal cap had diameter of 1.0 mm along the cone's axis, giving a total length of 5.5 mm. For each blood pool, the myocardial shape was determined with three wall thickness. For ED the wall thicknesses were selected to be of 0.75, 1.0, and 1.25 mm. For ES the wall thicknesses were determined by matching the myocardial volume of the corresponding ED peice, giving wall thickness values of 0.94, 1.22, and 1.51 mm, respectively.

These phantom dimensions were chosen to represent the size of the myocardium of a typical adult mouse. Fig. 2B shows three different sizes of ES myocardial parts, which are used in position 4 in Fig. 2A. The different sections were designed to fit into a pre-existing phantom tube and allow for filling of the entire phantom with a uniform concentration of activity. To assemble the phantom, the base myocardium, which has two narrow, solid rods extending the full length of the entire assembled phantom, is placed into the empty phantom tube and the myocardial cavity filled using a syringe. All subsequent pieces slide onto the two rods via the designed through-holes (seen in Fig. 2B), such that the pieces are properly aligned (Fig. 2C). Each piece is filled after being placed inside the tube, and after all pieces are in place, the phantom is fully filled to remove any air bubbles, and then closed. The phantom

4

is filled with a single syringe of activity, ensuring that all parts of the phantom have the same activity concentration.
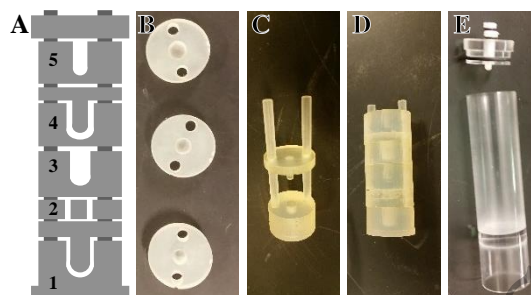

Fig. 2. The phantom design (A) contains ED myocardium (1), hot rod (2), ED blood pool (3), ES myocardium (4) and ES blood pool (5) sections. Gaps are shown between pieces for clarity. The hot rod section contains 6 equal-diameter, equally spaced rods and is not used in this work but was designed to demonstrate image resolution. Photographs (B-E) show the 3D printed phantom parts and tube for filling.

2.2. Data Acquisition

The phantom was filled and imaged three times, once for each set of LV dimensions. The fill solutions had ^{99m}Tc activity concentrations of 9.5, 6.6, and 4.5 mCi/mL, respectively, for the 0.75, 1.0, and 1.25 mm ED wall thickness values. The 0.75 ED phantom was imaged for a total of 5 hours, 1 hour per individual section, while the 1.0 and 1.25 ED phantoms were imaged for a total of 10 hours, 2 hours per individual section. All acquisition data were collected in list-mode on an MiLabs U-SPECT+ system, having a spatial resolution of approximately 0.45 mm (van der Have *et al.*, 2009).

All three acquisitions had between $5 \cdot 10^8$ and $8 \cdot 10^8$ photopeak counts. Each section of the phantom was imaged in a single bed position. The known configuration and dimensions of the phantom allowed us to translate the system bed in such a way that each subsequent compartment would be correctly positioned within the SPECT field of view (FOV) so that the projections properly aligned. This approach also permits synthesizing data according to any defined time-activity curve, allowing us to merge projection data from corresponding myocardial and blood-pool compartments after the temporal scaling operation. The combination of high activity and long acquisition time provided a sufficient number of events to divide a single long list-mode data set into multiple synthesized dynamic data frames.

2.3. Kinetic Modeling

The rate of uptake of the tracer from the blood pool into the myocardial tissue, referred to as K_1, can be used to determine myocardial blood flow (MBF). In this work, we utilized a 1-tissue compartment model, as shown in Fig. 3, where the tracer concentration in the blood pool, $C_a(t)$, is related to the tracer concentration in the myocardium, $C_t(t)$, by the rates K_1 and k_2. In this work, k_2 is assumed to be zero over the course of imaging because we are primarily interested in imaging tracers that are rapidly sequestered inside myocardial cells with little or no washout or recirculation, e.g., ^{99m}Tc-Sestamibi. Equation (1) represents this model mathematically, and was used in our software to estimate K_1 (Klein *et al.*, 2010).
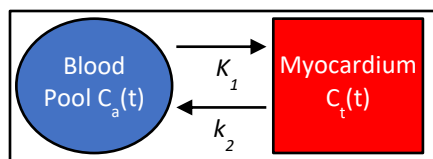
Fig. 3: Diagram of a one-tissue compartment model, showing the rates of tracer (K_1 and k_2) movement between the arterail blood pool and myocardial tissue.

$$\frac{dC_t(t)}{dt} = K_1 C_a(t) - k_2 C_t(t) = K_1 C_a(t) \text{ (for tracers with } k_2=0)$$ Eqn 1

Additionally, our kinetic modeling software allows for mixing between the blood pool and myocardial concentration estimates obtained from image regions of interest (ROI). The ROI drawn over the myocardium is composed of activity from the myocardium in addition to spillover from ventricles and blood pool due to resolution limitations and, in the case of animal imaging, myocardial wall motion. The blood pool ROI contains the activity inside the left ventricular blood pool and spillover from the myocardium, and also in the case of animal imaging would include spillover due to wall motion. The software accounts for this using a generalization of a mixing matrix (Klein *et al.*, 2010), as shown in Eqn. (2):

$$\begin{pmatrix} C_{Myo}(t) \\ C_{BP}(t) \end{pmatrix} = \begin{pmatrix} R_T & F_A \\ F_T & R_A \end{pmatrix} \begin{pmatrix} C_T(t) \\ C_A(t) \end{pmatrix}$$ Eqn 2

where $C_{Myo}(t)$ and $C_{BP}(t)$ are functions over time of mean activity concentration from ROIs drawn over the myocardium and blood pool, respectively, $C_T(t)$ and $C_A(t)$ are the true concentrations in the myocardial tissue and arterial blood over time, respectively, R_T and R_A are the constants representing the observed fraction of myocardial-tissue concentration seen within the myocardial ROI and the fraction of arterial-blood concentration seen in the left ventricular ROI. F_A and F_T are the constant fraction of spillover from the arterial blood into the myocardium, and from the myocardial tissue into the left ventricle blood pool, respectively. In a mouse, F_A can arise from both resolution and motion effects, as well as from blood perfusion within the heart muscle. The fitting algorithm, when provided with the inputs $C_{Myo}(t)$, $C_{BP}(t)$, R_T and R_A, uniquely estimates the resulting values of F_A, F_T, $C_T(t)$, $C_A(t)$, and K_1.

Typically, following determination of K_1, MBF is subsequently calculated numerically using the Renkin-Crone model as shown in Eqn. (3):

$$K_1 = MBF * EXF = MBF * \left(1 - e^{-\alpha} e^{-\beta/MBF}\right)$$ Eqn 3

where EXF is the extraction fraction, a tracer-specific quantity that accounts for nonlinear tracer extraction as a function of MBF and the effective capillary permeability times surface area product (Klein *et al.*, 2010). These parameters are condensed into α and β, for which values can be found in literature, such as α=0.14 and β=0.44 ml/min/g for ^{99m}Tc-sestamibi. These values were determined in an isolated isovolumetric contracting rabbit heart (Leppo and Meerdink, 1989) and we are unaware of measurements of mouse-specific values. Although these literature values for rabbits could be applied to mice studies, to avoid further inconsistencies being incorporated into results, this work will focus on the accuracy of determining K_1 instead of *MBF*.

2.4. Dynamic-Data Generation

Following raw-data acquisition, the static data from each single phantom compartment were combined and manipulated into synthetic dynamic data by randomly accepting events in proportions obtained from an assumed kinetic model, mimicking actual dynamic mouse acquisitions. A probability function

6

was used to accept or reject events from the original list-mode file to create each time frame of the dynamic time activity curve. A constant scale factor, λ, was used to control the fraction of events from the list-mode file in order to provide a count rate similar to that of animal studies. The blood pool and myocardial compartments have unique probability functions that mimic a typical animal acquisition. For each event in the corresponding myocardium or blood pool compartment data files, a uniformly distributed random number, U[0,1], was obtained from a standard computer random-number generator. If that number was less than the calculated probability constant at a particular time point, the event was used. The blood pool probability was determined using Eqn. 4, based on an assumed Gaussian shape for the input function, similar to what we have seen experimentally (Fig. 1):

$$P_{C_A}(t) = \lambda e^{-\frac{(t-t_0)^2}{2\sigma^2}} \qquad \text{Eqn 4}$$

where $P_{C_A}(t)$ is the probability "input function" of the arterial blood pool, t_0 is the peak time of the activity injection, λ is a scale factor to control the count level, and σ is the width (standard deviation) of the injection pulse. λ was chosen to give an appropriate number of counts and to ensure that the calculated probability was never greater than 1 at any time. A separate λ was determined for each phantom acquisition, but it was the same for both the myocardial and blood pool probability functions. Its value was determined by ensuring that an approximately equal number of events occurred for each phantom acquisition and were matched to an example mouse acquisition. Both t_0 (injection peak time) and σ (width of injection bolus) are constant for all protocols in this study.

For the myocardium probability, we impose the constraint of the 1-tissue compartment model from Eqn. 1, as seen in Eqn. 5:

$$P_{C_T}(t) = K_1 \int_0^t dt'\, P_{C_A}(t) = K_1 \lambda \int_0^t dt'\, e^{-\frac{(t'-t_0)^2}{2\sigma^2}} = K_1 \lambda \sigma \sqrt{\frac{\pi}{2}} \left[\text{erf}\left(\frac{t-t_0}{\sqrt{2}\sigma}\right) - \text{erf}\left(\frac{-t_0}{\sqrt{2}\sigma}\right)\right] \qquad \text{Eqn 5}$$

where $P_{C_T}(t)$ is the probability function of the myocardium and K_1 is the uptake rate of ^{99m}Tc-sestamibi from the blood into the myocardium (min^{-1}).

To mimic unpublished rest/stress animal data, the phantom data were processed into 5-min acquisitions with 10-second dynamic frames, with the center of injected activity occurring at 60 seconds into the scan – the actual injection would occur a few seconds prior to the peak in a mouse. For each phantom, the input K_1 value was set to be 0.5 min^{-1}, 1.5 min^{-1}, or 2.5 min^{-1} to represent rest and stress. These values were chosen as they fall within the expected range of values for mice (Croteau *et al.*, 2015). Both myocardial and blood pool probability functions are shown in Fig. 4. Both the simulated myocardial and blood pool probability functions are similar in shape to previously collected animal data, an example of which is shown in Fig. 1. The differences between the probability functions and the animal data are due to the limited dynamic sampling of the SPECT data in combination with spill-over between the blood pool and myocardium animal ROIs which is a result of both system resolution and cardiac motion.
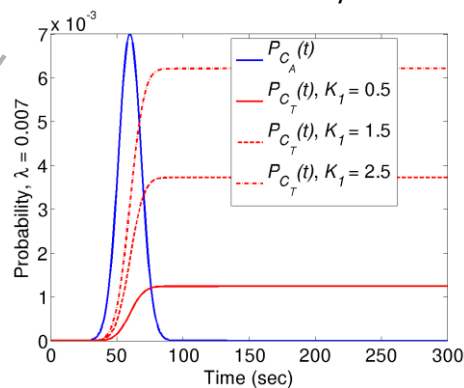
Fig. 4. Examples of the arterial and tissue probability functions for a five-minute acquisition with the injected activity peak occurring at 60 seconds, showing the three different K_1 values (0.5 min^{-1}, 1.5 min^{-1}, or 2.5 min^{-1}) used in this work to represent a range of rest and stress in mice.

2.4.1. Dynamic End Diastole and End Systole Image Ensemble Generation

To simulate the dynamic data, the equations above were averaged over the 10 seconds of each dynamic frame in 1-second steps, with λ chosen such that the myocardial concentration was approximately that obtained from mice rest/stress data (Guerraty *et al.*, 2017). The appropriate probability function was used for each part of the phantom, applying a half-life correction based on each part's acquisition start time. The resulting dynamic blood-pool and myocardial list-mode data were combined into a single dynamic data set and reconstructed using the USPECT+ system's reconstruction software. This gives, from a single phantom, three dynamic data sets: (1) the combined blood pool and myocardium for ES; (2) the combined blood pool and myocardium for ED; and (3) the mixed model of EDES which represents the data that might be obtained from a moving (beating) heart (described below). This process is illustrated in Fig. 5. This probability model was then re-applied 25 times for each phantom data set and K_1 input combination to create multiple noise ensemble image sets. Each individual noise ensemble set was created with the same probability function parameters (t_0, σ, λ, and K_1). Each phantom data set has a very small λ, all less than 0.01, which allows for statistically independent noise realizations.
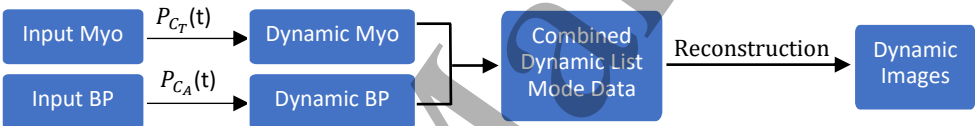

Fig. 5. Flow chart depicting the process of turning the original phantom's list-mode data into dynamic images.

2.4.2. Motion Estimation Ensemble Generation

To simulate basic cardiac motion, we used a combination of the raw data from both the ED and ES sections. In humans, it is typical for the myocardium to spend from 1/3 to 3/8 of the cardiac cycle in systole and the remaing time in diastole (Zipes *et al.*, 2014) . However, mice have a higher heart rate than humans and therefore spend less time in diastole. To compensate for this, we chose to pull events from the ED and ES compenents of the raw list-mode data in a ratio of 60% ED and 40% ES based on observations from unpublished mouse echo data. These data follow the same processing as shown in Fig. 5, except the 'Input Myo' and 'Input BP' boxes are the mixed ratio list-mode data.

2.5. Dynamic Data Processing

The static acquisitions of each phantom compartment were also individually reconstructed. This reconstruction was then used to define 3D ROIs for each phantom part (ED myocardium, ES myocardium, ED blood pool, ES blood pool). The ROIs were defined by including all voxels that have an intensity of 50% or higher of the maximum image intensity of the reconstructed images. Unique ROIs were defined for combination of iteration number and post-reconstruction filter value. ROIs were then applied to the ES and ED reconstructed images for each dynamic data set, including each phantom, each K_1 input value, and each ensemble noise realization. At each dynamic time point, the mean ROI value was determined and used to create time-activity curves. The time-activity curves were then used in our customized kinetic modeling software to estimate K_1 from the reconstructed images. For the motion-blurred EDES data the same method was used, except that the static, part-weighted data (60% ED, 40% ES) were reconstructed and used as the basis for the ROIs for the combined EDES ensembles.

8

2.5.1. Determining R_T and R_A fit inputs

To determine the required fitting constants R_T and R_A, we first calculated the true activity-concentration values in the myocardial tissue, $C_T(t)$, and in the arterial blood pool $C_A(t)$. First, utilizing the known activity concentration of the phantom, A, an effective activity concentration, A_{eff}, was calculated, correcting for the differences in the reconstructed phantom's frame duration, t_{frame}, and that of the phantom compartment in question, t_{acq}, as seen in Eqn. 6 and 7, where τ is the half-life of ^{99m}Tc:

$$A_{eff} \int_0^{t_{frame}} 2^{-t/\tau} \, dt = A \int_0^{t_{acq}} 2^{-t/\tau} \, dt \qquad \text{Eqn 6}$$

$$A_{eff} = A \frac{1 - 2^{\frac{-t_{acq}}{\tau}}}{1 - 2^{\frac{-t_{frame}}{\tau}}} \qquad \text{Eqn 7}$$

The effective activity concentration was then used to determine the true concentration of activity in the myocardium and blood pool using the probability functions defined in Eqn. 4 and 5, averaged over the 10-second frames where $\overline{P_{C_A}(t)}$ and $\overline{P_{C_T}(t)}$ are the average probability for the time frame containing t, as shown in Eqn. 8 and 9:

$$C_A(t) = \overline{P_{C_A}(t)} \, A_{eff} \qquad \text{Eqn 8}$$

$$C_T(t) = \overline{P_{C_T}(t)} \, A_{eff} \qquad \text{Eqn 9}$$

To determine R_T and R_A estimates, we used equations from the mixing matrix in Eqn. 2 and performed a least-squares minimization over all time frames as seen in Eqn. 10 and 11:

$$S_1 = \sum_{All\ Frames} [C_{BP}(t) - F_T C_T(t) - R_A C_A(t)]^2 \qquad \text{Eqn 10}$$

$$S_2 = \sum_{All\ Frames} [C_{MYO}(t) - R_T C_T(t) - F_A C_A(t)]^2 \qquad \text{Eqn 11}$$

where C_{Myo} and C_{BP} are parameters obtained based on R_A, R_T, F_A, and F_T.

Taking the derivative of Eqn. 10 with respect to R_A and F_T and Eqn. 11 with respect to R_T and F_A gives Eqn. 12 and 13, (F_T and F_A not shown):

$$R_A = \frac{\sum C_T C_A \sum C_T C_{BP} - \sum C_T^2 \sum C_{BP} C_A}{(\sum C_T C_A)^2 - \sum C_A^2 \sum C_T^2} \qquad \text{Eqn 12}$$

$$R_T = \frac{\sum C_T C_A \sum C_A C_{MYO} - \sum C_A^2 \sum C_{MYO} C_T}{(\sum C_T C_A)^2 - \sum C_A^2 \sum C_T^2} \qquad \text{Eqn 13}$$

2.6. Reconstruction and Fit Evaluation

Determining the optimal number of iterations and smoothing

As with most iterative reconstruction algorithms, determining a balance between reconstruction iteration number and smoothing can be difficult. In this work the optimization of the number of iterations and amount smoothing parameters with respect to K_1 accuracy allows for an estimate of error of K_1 and to also determine if, and how much, different K_1 values both the optimized reconstruction parameters and the resulting K_1 error. For this work, we reconstructed each noise ensemble and K_1 combination of phantom acquisition to determine an optimal iteration and smoothing combination. Each data set was reconstructed with 11 different smoothing parameters, using a Gaussian filter of 0, 0.1, 0.2, 0.3, 0.4, 0.5, 0.6, 0.7, 0.8, 0.9, or 1.0 mm standard deviation, and for each of 20 iterations, always using 4 subsets. A separate ROI for each iteration and smoothing combination was determined by using 50% of the maximum of the individually-reconstructed static phantom segments for a matched number of iterations and smoothing parameter value. R_A and R_T were determined as described above for each noise instance, smoothing and iteration combination. For each smoothing and iteration combination, the mean of R_A and R_T over all noise realizations was determined and used as an input into the fitting software in conjunction with the ROI-determined time activity curves. The MSE error of K_1

9

value returned by the fit compared to the input ground truth was then used as a metric to determine the optimal levels of smoothing and number of iterations.

2.6.1 Sensitivity of K_1 to R_T and R_A

As R_T and R_A are required as an input into our fitting software, understanding the error associated with their estimate is critical for understanding their effects on the fitting accuracy of K_1 and subsequently MBF. In this phantom study, we accurately estimate both R_T and R_A, which includes effects due to resolution and partial-volume spillover. In mice, this evaluation is more challenging, as it not only includes effects of resolution and spillover, but also the effect of cardiac motion. To estimate the effect of inaccurate R_T and R_A on K_1 accuracy, we can compare the kinetic modeling fits of the perfect R_T and R_A values calculated from equations 12 and 13 for each noise realization from that of results when the mean R_T and R_A of the 25 noise realizations is used.

3. Results

This work first establishes that a single phantom acquisition can be turned into synthetic dynamic data which can be subsequently used as input into kinetic modeling software for determination of K_1. Next, it investigates the effect of the input R_T and R_A values on K_1 accuracy taking into consideration the different phantom types (ED, ES, and EDES-combination), iteration number and smoothing amount. Finally, we evaluate the accuracy of K_1 in a variety of cases in order to gain insight into the amount of error from system noise and the kinetic modeling software. This allows for understanding of the limitations of kinetic modeling when moving to *in-vivo* mice studies.

3.1. Dynamic Data Example

A short, full-phantom acquisition was imaged and reconstructed to allow for visualization of the entire phantom and is shown in Fig. 6. Each phantom compartment is clearly visualized, along with activity that can be seen along the edges and near the lid of the phantom tube.

Fig. 6: Coronal slice of the entire cardiac phantom with an ED wall thickness of 1.25 mm (10 iterations, 0.25 FWHM post-filter), showing, from bottom to top, the ED myocardium, ED blood pool, ES myocardium, and the ES blood pool.

The results from a single noise realization of the dynamic data-processing scheme are shown in Fig. 7 for the 1.25 mm ED phantom size, K_1 of 0.5 min^{-1}, reconstructed with no filtering for 20 iterations with 4 subsets.
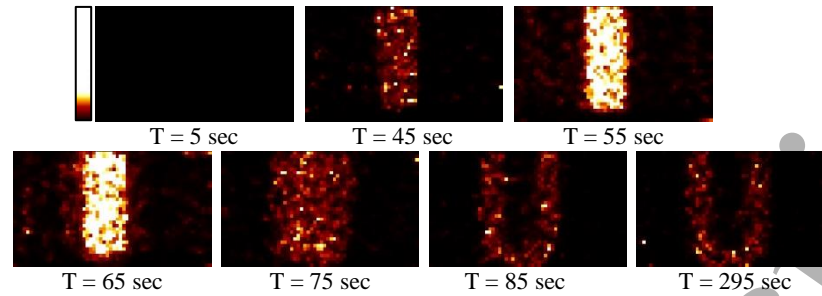
Fig. 7: Central slice of reconstructed dynamic data over time, visualizing the wash-in and wash-out of the myocardial and blood-pool compartments.

For the same data set as in Fig. 7, the previously determined ROIs for the blood pool and myocardium were applied and used to determine the required input into the kinetic modeling software. The program was then run using the average of the R_A and R_T values determined from equations 12 and 13, for the noise ensemble, 0.841 and 0.839 respectively, for the particular iteration number and filter value. The resulting arterial and tissue components were then determined by the kinetic modeling software, with the resulting time-activity curves shown in Fig. 8.
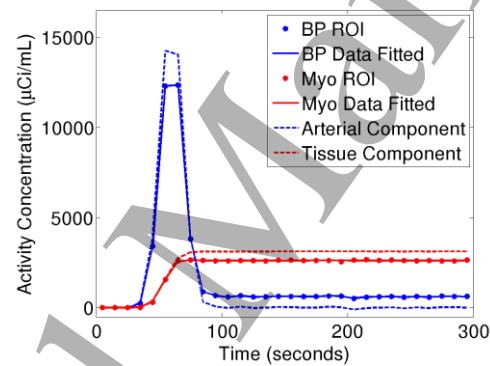

Fig. 8: Example time-activity curves showing input into the kinetic modeling software including the blood pool ROI (BP ROI), myocardial ROI (Myo ROI), their fitted input curves (BP Data Fitted and Myo Data Fitted), and the resulting separated curves (dotted lines) that were used to determine K_1.

3.2. Variation of R_T and R_A

For each reconstruction setting, including the iteration number, filter parameter, phantom type (ED, ES and motion-estimating EDES combination), wall thickness (0.75, 1.00, and 1.25 mm), K_1 (0.5, 1.5, and 2.5 min^{-1}), and noise realization, R_T and R_A were determined from equations 12 and 13. Fig. 9 shows an example of a histogram of the noise ensemble of the determined R_T and R_A values for the ED phantom with a wall thickness of 0.75 mm, K_1 of 0.5, and no filtering, at two different iteration numbers. Visual inspection shows that the R_T and R_A values obtained from the different noise realizations were grouped quite tightly for each number of iterations, and that increasing iterations changed the values of the recovery coefficients. The results of other phantom and reconstruction combinations were similar (not shown).
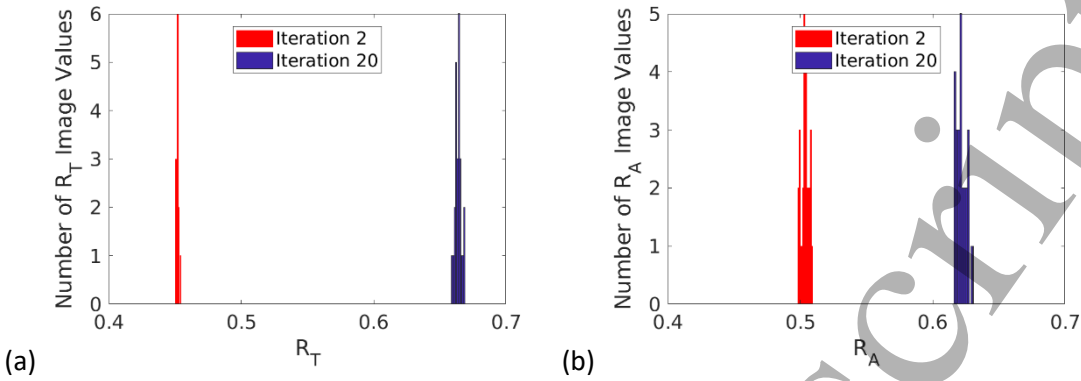
Fig. 9: Histograms of noise ensembles of determined R_T (a) and R_A (b) values for the ED phantom with a wall thickness of 0.75 mm, K_1 of 0.5 min^{-1}, and no filtering.

In addition to looking at the individual R_T and R_A values, it is useful to determine if there are differences at the noise-ensemble level. These data allow for better understanding of how differences in R_T and R_A values may affect quantification in animal studies if inaccurate R_T and R_A values are utilized. Therefore, Fig. 10 and Fig. 11 show both the mean and percent standard deviation of R_T and R_A values, respectively for a variety of different phantom and reconstruction combinations. All results are in the expected range of zero to one, where one would imply a perfect reconstruction with complete recovery of all activity falling within the ROI. The mean R_T and R_A values mostly stabilize after five iterations, and comparing across different extremes of filtering, wall thickness and part type do not affect the general trends of the mean values.
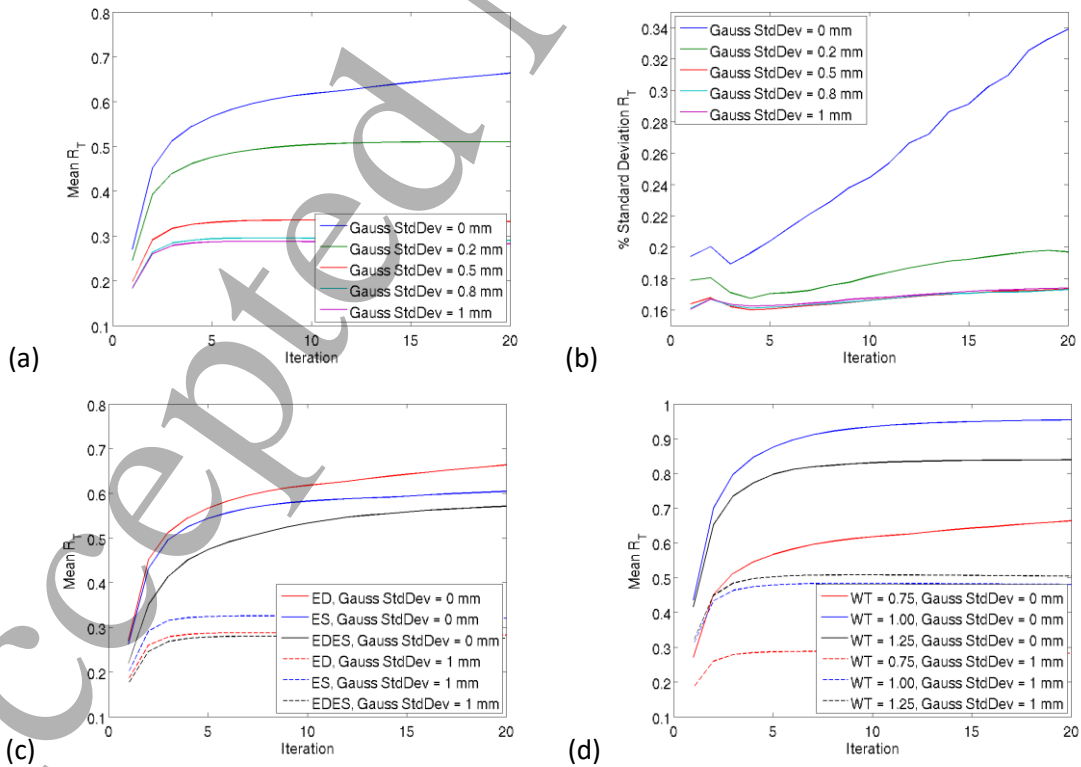
12

Fig. 10: The mean (a) and percent standard deviation (b) of the noise-ensemble R_T values for the ED phantom with a wall thickness of 0.75 mm over iteration and varying Gaussian filtering. To compare across phantom types, (c) shows the mean R_T across the three different phantom types (ED, ES and EDES motion-estimation) at two different filter levels for the 0.75 mm wall thickness and K_1 of 0.5 min^{-1}. Similarly, (d) compares the mean R_T across varying wall thickness at two different filter levels for the ED part type and K_1 of 0.5 min^{-1}.
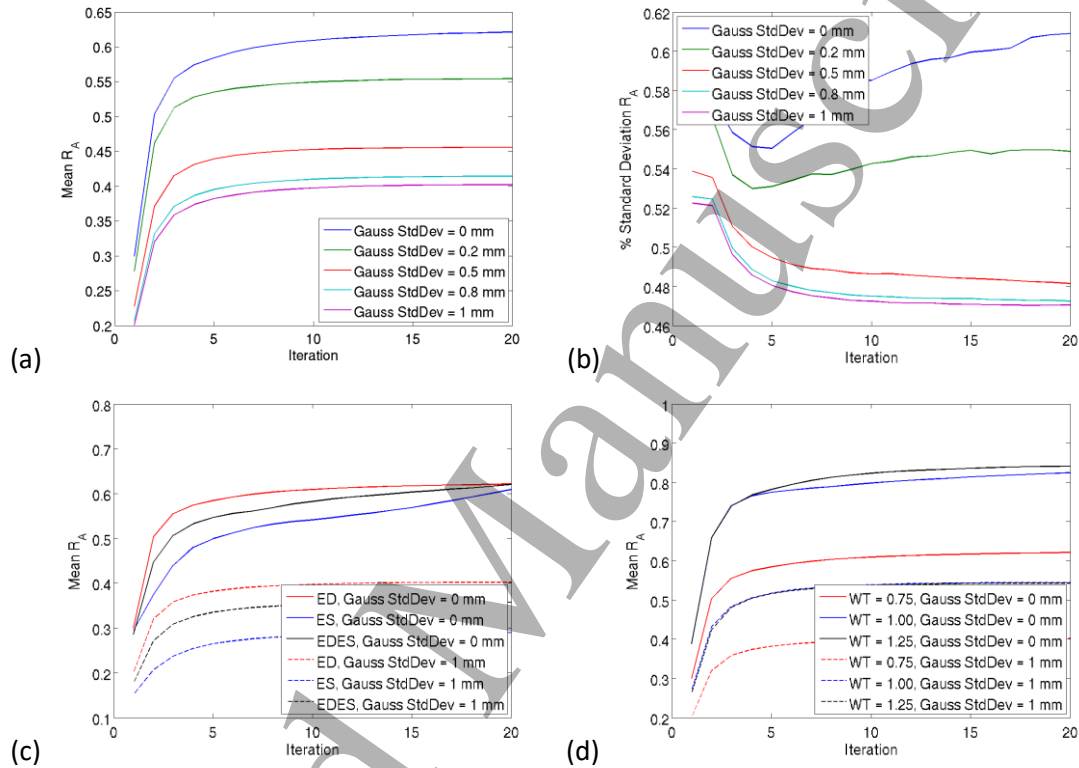

(a)

(b)

(c)

(d)

Fig. 11: The mean (a) and percent standard deviation (b) of the noise-ensemble R_A values for the ED phantom with a wall thickness of 0.75 mm over iteration and varying Gaussian filtering. To compare across phantom types, (c) shows the mean R_A across the three different phantom types (ED, ES and EDES motion-estimation) at two different filter levels for the 0.75 mm wall thickness and K_1 of 0.5 min^{-1}. Similarly, (d) compares the mean R_A across varying wall thickness at two different filter levels for the ED part type and K_1 of 0.5 min^{-1}.

Similar to plots shown in Fig. 10 and 11, Fig. 12 and Fig. 13 show trends of R_T and R_A, respectively, across different phantom sizes. Fig. 12 shows that R_T is lower for the 1.25 mm wall thickness phantom compared to the 1 mm phantom while Fig. 13 shows that R_A for 1.25 mm wall thickness phantom is similar or slightly higher compared to the 1 mm phantom.
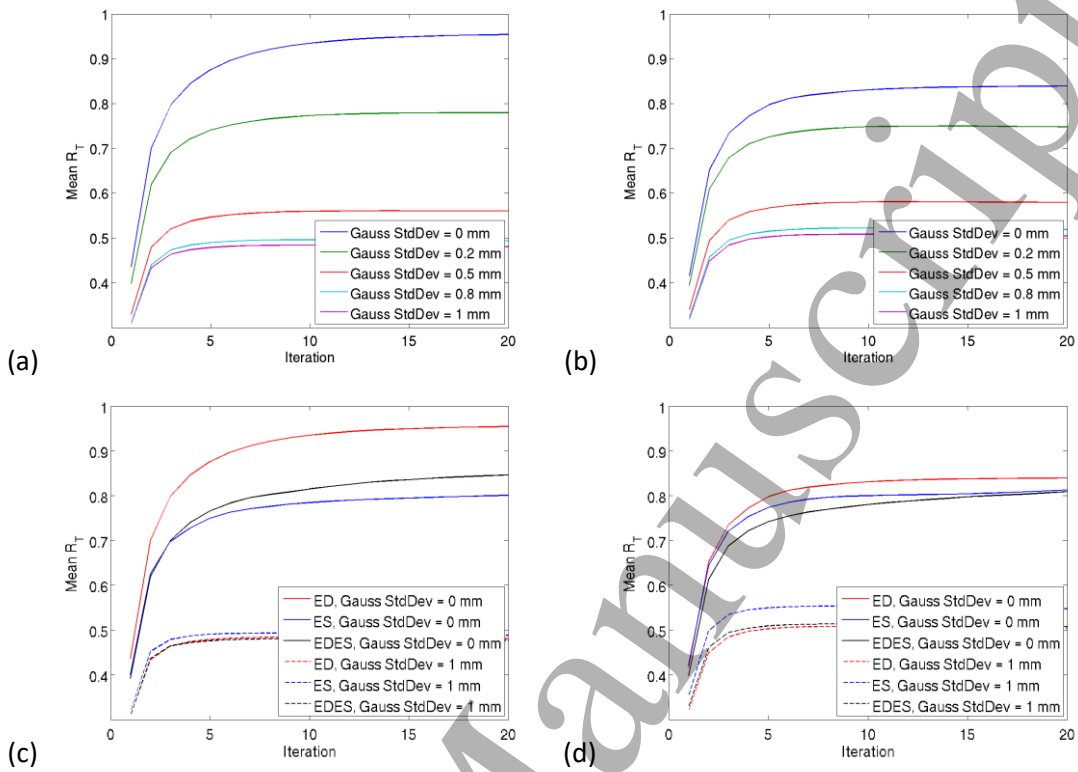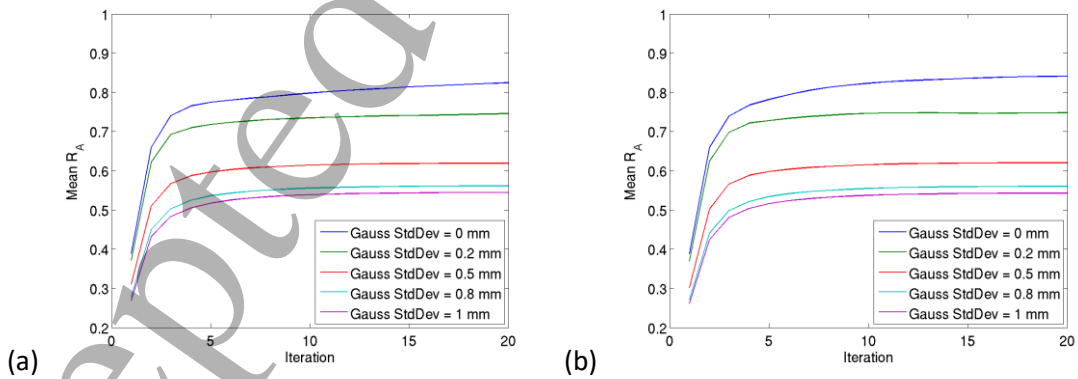
13

(a)

(b)

(c)

(d)

Fig. 12: The mean of the noise-ensemble R_T values for the ED phantom with a wall thickness of (a) 1 mm and (b) 1.25 mm over iteration and varying Gaussian filtering. To compare across phantom types, (c) and (d) show the mean R_T across the three different phantom types (ED, ES and EDES motion-estimation) for the 1.0 and 1.25 mm wall thickness, respectively, at two different filter levels and K_1 of 0.5 min^{-1}.
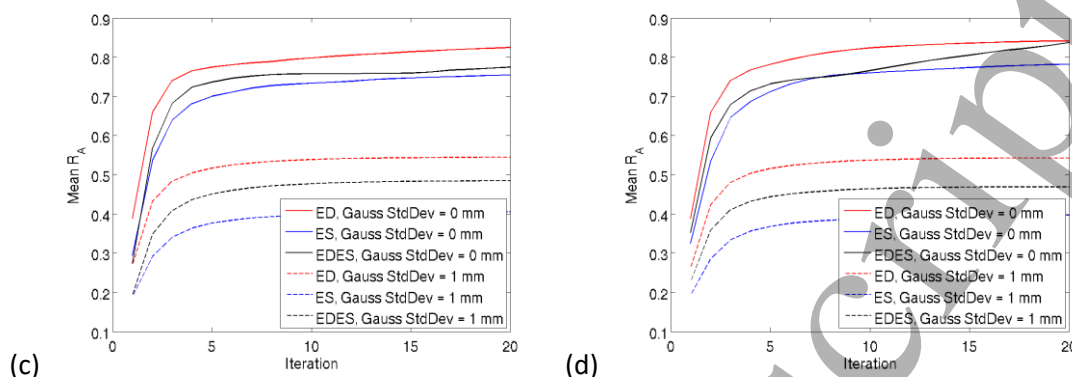

(a)

(b)

Fig. 13: The mean of the noise-ensemble R_A values for the ED phantom with a wall thickness of (a) 1 mm and (b) 1.25 mm over iteration and varying Gaussian filtering. To compare across phantom types, (c) and (d) show the mean R_A across the three different phantom types (ED, ES and EDES motion-estimation) for the 1.0 and 1.25 mm wall thickness, respectively, at two different filter levels and K_1 of 0.5 min^{-1}.

3.3. Evaluation of K_1 Accuracy

To estimate error in the accuracy of K_1 estimation, the mean value of R_T and R_A determined for each noise ensemble (instead of each determined R_T and R_A values from equations 12 and 13) were used as inputs into the kinetic modeling software in conjunction with the original time activity curve inputs. This allows for an estimation of how accurate K_1 error is when population-average values of R_T and R_A are used, as is likely to occur when imaging animal subjects. Additionally, this allows for insight into an appropriate number of iterations and amount of smoothing for the noise-level of images produced in this study. Fig. 14 shows the percent root-mean-square error (% RMSE) for a phantom noise ensemble of the ED phantom with a wall thickness of 0.75 mm and a K_1 of 0.5 min^{-1} by both filter amount and iteration. Increasing the number of iterations decreases the % RMSE, while less filtering also decreases the % RMSE. This trend is similar across all phantom types, wall thicknesses, and K_1 values (data not shown). This implies that for the most accurate quantification, more iterations and limited filtering is desired. To better visualize the range of error, for the 20th iteration and no filtering, Fig. 15 shows the K_1 % RMSE for each phantom type across each of the three K_1 values for each of the different wall thicknesses. The values range from less than 1% to 3.5%. The highest error is associated with the smallest wall thickness, which could be due to image resolution.
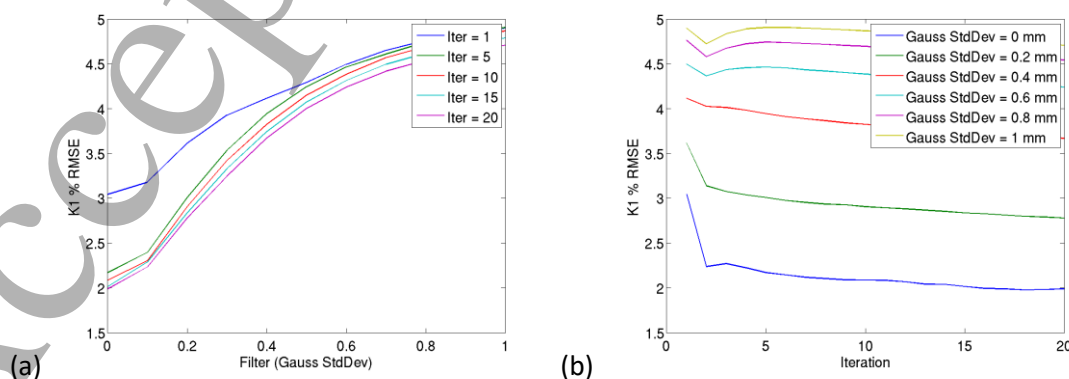
Fig. 14: The percent RMSE of K_1 when run with the mean R_T and R_A as input into the kinetic modeling software for the ED phantom with a wall thickness of 0.75 mm and a K_1 of 0.5 min^{-1}. The results are shown by both amount of filtering (a) and iteration (b).

(a)   (b)
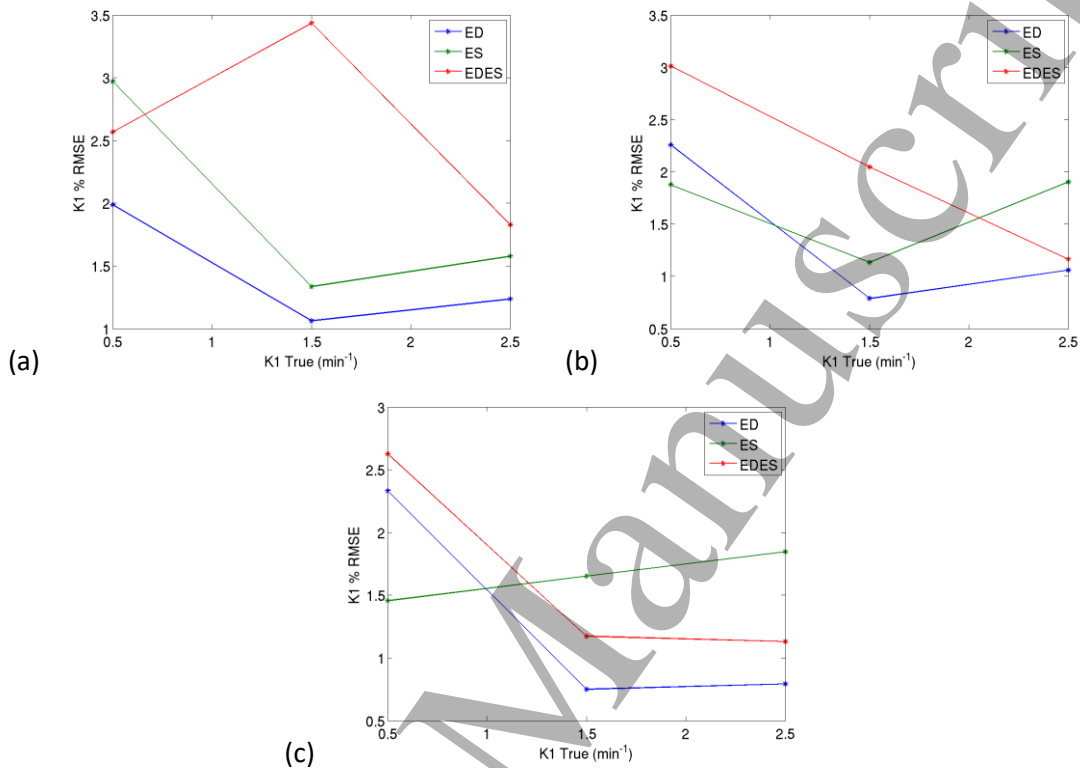

(c)

Fig. 15: The K_1 percent RMS is shown for each phantom part combination (ED, ES, and EDES motion-approximation) at wall thicknesses 0.75, 1.00, and 1.25 for (a), (b) and (c), respectively.

4. Discussion and Conclusion

This work demonstrates that for the modeled cardiac phantom, reasonable error (~3% RMSE) in estimation of tracer uptake rate is possible for the U-SPECT+ system used in this study over several uptake rates and LV dimensions. This error includes effects of system noise and resolution on reconstructed images. The main benefit of using this method to assess the tracer uptake rate is that there is a known ground truth that can be used to evaluate accuracy.

Figure 9 shows that the values for the recovery coefficients, R_T and R_A, have a small variance, but the mean varies as a function of iteration for the ED phantom. Figure 10 reinforces that and shows that the values for these fitting parameters converge within about 20 iterations. The converged values, unsurprisingly, depend on the amount of post filtering. Similar results are seen in Figure 11 for the ES phantom.

Figures 12 and 13 show trends of R_T and R_A, respectively, across different phantom sizes. Fig. 12 shows that there is some variation in R_T across different wall thicknesses, but no clear trends are present. Fig 13 shows that there is little difference across wall thickness sizes for R_A, implying that the location and size of the LV ROI makes the results mostly independent of wall thickness

16

Figure 14 shows the Root-Mean-Squared (RMS) Error for K_1. The uncertainty in K_1 increases with more post filtering. The uncertainty decreases with number of iterations. This latter observation is consistent with the results of Figures 9-11, indicating the stability of the mixing parameters at higher iteration. The former observation, especially in combination with the observation on number of iterations, suggests that sharper images give more quantitatively accurate measurements for this application. Further, although one cannot conclude that the quantification is optimized at 20 iterations, it is clear from Fig. 14 that the RMSE at 20 iterations is likely very close to the asymptotic limit for reasonable computational time for the reconstructions.

Figure 15 shows that the minimized RMS error for K_1 is about 2-3% for the range of K_1 values and configurations studied. It is difficult to discern consistent trends, suggesting that the noise on the data points is masking those trends.

The current phantom was designed to mimic cardiac imaging of wild-type mice of different sizes. A more disease-relevant model, which is achievable via 3D printing, would incorporate a myocardial lesion. Determination of the effect of a lesion on the estimation of K_1 would allow for additional understanding of the sensitivity of SPECT's ability to detect lesions, or changes in lesions, in small animals. This would be especially useful when evaluating treatment studies of disease models.

Although this work focuses on the dynamics of a particular tracer (^{99m}Tc – Sestamibi) and using the U-SPECT+ system, one advantage to this phantom and the processing methodology is that it can easily be applied to other imaging tracers, including PET tracers and systems. Future work could allow for comparison of quantification accuracy between these different tracers and systems to assess which is likely to give the most accurate and precise results. Additionally, our current kinetic modeling assumes that k_2 is zero, which – though a valid assumption for Sestamibi – is not true for all tracers. The manner in which data are modeled in this work easily allows for the myocardial and blood pool probability curves to be changed to accommodate more complicated kinetic models, such as those with more compartments. All that is required is to change Eqns. 4 and 5 which are used to generate the list-mode image data.

Other changes to the input probability curves (Eqns. 4 and 5) in future work could allow for more accurate modeling of biological processes and its effects in downstream accuracy. For example, in unpublished work, we have previously evaluated R_T in mice by excising the myocardium directly after imaging and R_A in a separate group of mice by labeling of red blood cells. In the process of this work, we have estimated the fraction of blood that is present in the myocardial tissue. This blood fraction could be incorporated into to the input probability curve to better mimic real conditions of potential error.

Although this work currently focuses on a single small-animal SPECT system, the use of a phantom to estimate the quantitative capabilities of dynamic imaging has great potential to evaluate sources of error not only in the field of small-animal cardiac applications, but also in other applications for which different phantoms could be designed. It is highly likely that the optimal reconstruction parameters of other SPECT or PET systems would follow the same trends of seeking image sharpness for quantification. Further, this phantom could be used to determine the values of mixing parameters as a function of heart size and adjust those parameters per mouse for more accurate results. In summary, the phantom is very useful for developing quantification related to kinetic modeling of flow tracers in a mouse heart.

This work has several limitations. First, the shape of the blood-pool curve is an estimate of a typical injection curve. This limits the application of these results to cases with similar injection curves and

would not extend to cases where a poor or unusual injection may substantially change the shape of the input function. These types of injections are likely to be excluded from most robust studies.

Another limitation of this work is that the spillover fractions are dependent on the ROI used for analysis. There are a variety of different ways one can draw a ROI on images, but determining them based on 50% of the maximum is a repeatable method that allows for consistency across all of the different reconstructions in this phantom study. Using a different method would likely change the resulting mixing parameters, but the focus of this work is on how the range of these values effects the accuracy of K_1 determination. It is not expected that changing the ROI method would vastly change the accuracy of K_1. Additionally, this method of ROI determination would not be applied to images with heterogenous uptake in the myocardium, as it would fail to include regions of low uptake. Alternative methods of ROI determination would need to be used to properly address this, and would likely involve hand-drawn or semi-automated methods similar to those currently used in animal and human imaging.

Additionally, the current method used to estimate motion does not fully capture the true motion during a heartbeat. The weighted-average of the two different positions provides at least some idea of the what the influence of motion would be, but further conclusions about motion would require methods that better estimate the stages between ED and ES, in addition to the final ED and ES positions.

In conclusion, we have designed and utilized a cardiac phantom to evaluate the robustness of our dynamic SPECT imaging capabilities. We have determined the necessary input parameters R_T and R_A for our kinetic modeling software and evaluated the effect of uncertainty in these values on the kinetic-fit results for K_1. This shows that these methods are likely to be useful in mice even when using estimated values of R_T and R_A. We determined that reconstruction using a relatively high number of iterations with minimal post-filtering led to the lowest errors on the estimates of K_1. Finally, there is a wide variety of additional studies and applications for which this phantom could be utilized.

References
Ahmed B 2014 New insights into the pathophysiology, classification, and diagnosis of coronary microvascular dysfunction *Coronary Artery Disease* **25** 439-49
Bairey Merz C N, Pepine C J, Walsh M N and Fleg J L 2017 Ischemia and No Obstructive Coronary Artery Disease (INOCA) *Developing Evidence-Based Therapies and Research Agenda for the Next Decade* **135** 1075-92
Beekman F and van der Have F 2007 The pinhole: gateway to ultra-high-resolution three-dimensional radionuclide imaging *European Journal of Nuclear Medicine and Molecular Imaging* **34** 151-61
Camici P G and Crea F 2007 Coronary Microvascular Dysfunction *New England Journal of Medicine* **356** 830-40

18

Chintalgattu V, Rees M L, Culver J C, Goel A, Jiffar T, Zhang J, Dunner K, Pati S, Bankson J A, Pasqualini R, Arap W, Bryan N S, Taegtmeyer H, Langley R R, Yao H, Kupferman M E, Entman M L, Dickinson M E and Khakoo A Y 2013 Coronary Microvascular Pericytes Are the Cellular Target of Sunitinib Malate–Induced Cardiotoxicity *Science Translational Medicine* **5** 187ra69-ra69

Croteau E, Renaud J M, McDonald M, Klein R, DaSilva J N, Beanlands R S and deKemp R A 2015 Test-retest repeatability of myocardial blood flow and infarct size using (1)(1)C-acetate micro-PET imaging in mice *Eur J Nucl Med Mol Imaging* **42** 1589-600

Duncker D J and Bache R J 2008 Regulation of Coronary Blood Flow During Exercise *Physiological Reviews* **88** 1009-86

Farhad H, Dunet V, Bachelard K, Allenbach G, Kaufmann P A and Prior J O 2013 Added prognostic value of myocardial blood flow quantitation in rubidium-82 positron emission tomography imaging *Eur Heart J Cardiovasc Imaging* **14** 1203-10

Gervais M, Démolis P, Domergue V, Lesage M, Richer C and Giudicelli J-F 1999 Systemic and Regional Hemodynamics Assessment in Rats with Fluorescent Microspheres *Journal of Cardiovascular Pharmacology* **33** 425-32

Gibson C M, Cannon C P, Murphy S A, Ryan K A, Mesley R, Marble S J, McCabe C H, Van de Werf F and Braunwald E 2000 Relationship of TIMI Myocardial Perfusion Grade to Mortality After Administration of Thrombolytic Drugs *Circulation* **101** 125-30

Guerraty M A, Johnson L C, Blankemeyer E, Wang T, Mankoff D A, Metzler S D and Rader D J 2017 Abstract 19007: Multimodality Blood Flow Imaging in Mice *Circulation* **136** A19007-A

Herzog B A, Husmann L, Valenta I, Gaemperli O, Siegrist P T, Tay F M, Burkhard N, Wyss C A and Kaufmann P A 2009 Long-term prognostic value of 13N-ammonia myocardial perfusion positron emission tomography added value of coronary flow reserve *J Am Coll Cardiol* **54** 150-6

Johnson L, Guerraty M, Blankemeyer E, Mankoff D, Rader D and Metzler S 2016 Small-animal SPECT dynamic cardiac imaging *Journal of Nuclear Medicine* **57** 122

Klein R, Beanlands R S B and deKemp R A 2010 Quantification of myocardial blood flow and flow reserve: Technical aspects *Journal of Nuclear Cardiology* **17** 555-70

Leppo J A and Meerdink D J 1989 Comparison of the myocardial uptake of a technetium-labeled isonitrile analogue and thallium *Circulation Research* **65** 632-9

Majmudar M D, Murthy V L, Shah R V, Kolli S, Mousavi N, Foster C R, Hainer J, Blankstein R, Dorbala S, Sitek A, Stevenson L W, Mehra M R and Di Carli M F 2015 Quantification of coronary flow reserve in patients with ischaemic and non-ischaemic cardiomyopathy and its association with clinical outcomes *European Heart Journal - Cardiovascular Imaging* **16** 900-9

Moslehi J, Minamishima Y A, Shi J, Neuberg D, Charytan D M, Padera R F, Signoretti S, Liao R and Kaelin W G 2010 Loss of Hypoxia-Inducible Factor Prolyl Hydroxylase Activity in Cardiomyocytes Phenocopies Ischemic Cardiomyopathy *Circulation* **122** 1004-16

Murthy V L, Naya M, Taqueti V R, Foster C R, Gaber M, Hainer J, Dorbala S, Blankstein R, Rimoldi O, Camici P G and Di Carli M F 2014 Effects of Gender on Coronary Microvascular Dysfunction and Cardiac Outcomes *Circulation*

van der Have F, Vastenhouw B, Ramakers R M, Branderhorst W, Krah J O, Ji C, Staelens S G and Beekman F J 2009 U-SPECT-II: An Ultra-High-Resolution Device for Molecular Small-Animal Imaging. *Journal of Nuclear Medicine* **50** 599-605

Zipes D P, Libby P, Bonow R O, Mann D L and Tomaselli G F 2014 *Braunwald's Heart Disease: A Textbook of Cardiovascular Medicine* (Philadelphia, PA: Saunders/Elsevier)